

CoMoO₄ Supported by N-doped Carbon Derived from ZIF-67 as a Novel Electrode Material for High Performance Supercapacitors

Hengzheng Li^{1,2}, Yanjiang Li^{1,2}, Guangzhen Zhao^{1,2}, Conghu Liu^{1,2}, Li Li^{1,2}, Guang Zhu^{1,2*}

¹ College of Mechanical and Electrical Engineering, Suzhou University, Suzhou 234000, Anhui, China;

² Key Laboratory of Spin Electron and Nanomaterials of Anhui Higher Education Institutes, Suzhou University, Suzhou 234000, Anhui, China

*E-mail: guangzhu78@126.com

Received: 9 June 2020 / Accepted: 27 July 2020 / Published: 31 August 2020

ZIF-67 derivatives show promising applications in energy storage owing to their high surface area and excellent electrochemical performance. In this work, an N-doped carbon-coated CoMoO₄ nanoparticle (CMO@NC) polyhedron was prepared by hydrothermal treatment and calcination. The structural and morphological properties of the obtained samples were measured by X-ray diffraction (XRD), scanning electron microscopy (SEM) and N₂ adsorption/desorption isotherms. In terms of electrochemical performance, CMO@NC exhibits a remarkable specific capacitance of 267.3 F g⁻¹ at 0.5 A g⁻¹. Moreover, a hybrid supercapacitor device with CMO@NC as the positive electrode material and active carbon (AC) as the negative electrode material was observed to achieve a specific capacitance of 114 F g⁻¹ at 0.5 A g⁻¹, with a stable operational voltage of 1.5 V and a maximum energy density of 35.4 Wh kg⁻¹ at a power density of 1041 W kg⁻¹. The specific capacitance retention can reach up to 82.4 % after 5000 cycles, as determined by GCD measurements, indicating outstanding cycling stability and potential application prospects in supercapacitors.

Keywords: Asymmetric supercapacitor; CoMoO₄@NC; Composite; High-performance

1. INTRODUCTION

In modern society, environmental issues and the energy crisis have become more serious with the development of industry. To take full advantage of renewable energy sources such as wind, solar and geothermal energies, electrochemical energy storage technology has attracted a considerable amount of attention owing to its potential applications in large-scale energy storage systems [1]. As dominant energy storage devices, supercapacitors (SCs) bridge the gap between traditional batteries and capacitors and have received prominent interest in electrical vehicles and grid storage systems due to their high

specific capacity and power density. In addition, SCs show a fast charge/discharge rate, high efficiency and long cycling life performances [2]. However, SCs display relatively low energy density. It is necessary to improve the energy density of SCs to meet the demand for large-scale energy storage systems.

Generally, an effective approach to improve the performance of SCs is to design and construct suitable electrode materials. Recently, pseudocapacitors (PCs) based on pseudocapacitive mechanisms with metal oxide electrode materials have gained increasing attention because their energy density is higher than those of electric double layer capacitors (EDLCs) [1, 3]. Among the currently reported metal oxides, Co_3O_4 has been widely investigated as a promising electrode for SCs because of its abundance, low cost for synthesis and excellent electrochemical activity [4]. Despite the progress achieved to date, practical applications are hindered by its pristine low electronic conductivity and poor cyclic stability, especially for fast charge/discharge processes. To overcome this problem, many studies have been conducted to prepare novel electrode materials, such as carbon coatings, metal element doping and composite electrode materials for Co_3O_4 .

Combining Co_3O_4 nanoparticles with carbon materials is considered an effective approach to solve the above issues due to the advantages of the carbon layer, including mechanical and chemical stability, a large specific surface area, and superior electric conductivity. Coating electrode materials with carbon can provide buffer voids and increase electric conductivity, thus resulting in excellent electrochemical performance. Many studies have been performed to construct carbon-coated metal oxide electrode materials via mechanical lapping, chemical vapor deposition and sol-gel processes [5-8]. For example, Kim et al. and Kazemi et al. reported hierarchical CoMoO_4 NPAs grown directly on nickel foam and dandelion-shaped CoMoO_4 nanostructures (ND- CoMoO_4) by a facile hydrothermal method, respectively, which have been used as electrodes for SCs [9][10]. In addition, Han et al. synthesized 2D hollow CoMoO_4 ultrathin nanosheets grown on conductive substrates, which achieved good electrochemical properties as electrodes for SCs [6]. However, these routes are limited in their applications because they involve toxic agents or complicated processes. Thus, it is highly desirable to develop a new approach for effectively fabricating carbon-coated Co_3O_4 electrode materials.

Recently, as one of the typical organic-inorganic hybrid materials, metal-organic frameworks (MOFs) have been widely used as effective precursors for in situ fabrication of carbon-coated electrode materials owing to their tunable chemical compositions and various structures. Previous studies have reported that MOFs are used as precursors to prepare different carbon-coated metal oxide materials [11]. In particular, $\text{Co}_3\text{O}_4@\text{NC}$ derived from ZIF-67 possesses the advantages of both N-doped content and high specific surface area, showing good capacitance [12, 13]. Very recently, Mo-doped pseudocapacitive metal oxides have greatly improved capacitance performance and cycling stability. Flower-like NiMoO_4 electrode materials were synthesized through reflux and subsequent heat treatment methods and showed a high capacity of 789 F g^{-1} and a capacity retention of 80.1 % after 2000 cycles [14]. Guo et al. prepared NiMiO_4 nanowires via a hydrothermal method based on nickel foam as the precursor, which displays high specific capacity at a very high current density and excellent cyclic stability [15]. Taking these advantages into consideration, Mo-doped carbon-coated Co_3O_4 derived from ZIF-67 should be suitable as an excellent electrochemical performance for supercapacitor applications.

In this work, a CoMoO_4 -decorated N-doped carbon matrix ($\text{CoMoO}_4@\text{NC}$) was proposed by annealing ZIF-67 as a precursor under a nitrogen atmosphere. As expected, the $\text{CoMoO}_4@\text{NC}$ composites showed a considerable improvement in electrochemical performance as SC electrode materials. They displayed a specific capacitance of 263.7 F g^{-1} at 0.5 A g^{-1} in 6 M KOH electrolyte. Furthermore, the hybrid SCs exhibited a specific capacitance of 114 F g^{-1} at 0.5 A g^{-1} , an excellent rate performance of 5 F g^{-1} at 20 A g^{-1} , and superior long cycling stability with a retention of 82.4 % after 5000 cycles.

2. EXPERIMENTAL

2.1 Synthesis of ZIF-67 precursor and $\text{Co}@\text{NC}$

All chemical agents were obtained from Sinopharm Reagent Group, were of analytical grade, and were used without further purification. In a typical process, 4 mmol 2-methylimidazole was dissolved in 15 mL methanol to form solution A, and 2.5 mmol $\text{Co}(\text{NO}_3)_2 \cdot 6\text{H}_2\text{O}$ was dissolved in 15 mL methanol to form solution B. Then, solution B was quickly poured into solution A and subjected to vigorous magnetic stirring at room temperature for 30 min. After reaction for more than 24 h without any disturbance, the bluish violet precipitate was collected via centrifugation, washed with methanol several times, and then dried at $80 \text{ }^\circ\text{C}$ for further use. For preparation of $\text{Co}@\text{NC}$, the as-prepared ZIF-67 was carbonized at $600 \text{ }^\circ\text{C}$ for 2 h in a N_2 atmosphere at a heating rate of $1 \text{ }^\circ\text{C min}^{-1}$ to obtain the desired $\text{Co}@\text{NC}$.

2.2 Synthesis of $\text{CoMoO}_4@\text{NC}$

First, as-prepared $\text{Co}@\text{NC}$ (0.2 g) was dispersed into 60 mL deionized water under ultrasonic excitation. Then, $\text{Na}_2\text{MoO}_4 \cdot 2\text{H}_2\text{O}$ (0.4839 g) and $\text{CoCl}_2 \cdot 6\text{H}_2\text{O}$ (0.4758 g) were added into the dispersed solution with constant stirring for 30 min. Finally, the dispersed solution was transferred into a 100 mL polytetrafluoroethylene Teflon-lined stainless-steel autoclave and heated at $160 \text{ }^\circ\text{C}$ for 2 h. After cooling to room temperature, the obtained sample was collected by centrifugation and washed with ethanol and deionized water several times. The final products were obtained and donated as $\text{CMO}@\text{NC}$.

2.3 Characterization

The morphologies and structure of the as-prepared samples were determined by field emission scanning electron microscopy (FESEM, JEOL JSM-LV5610). The physical and chemical properties of the composites were measured by X-ray diffraction spectroscopy (XRD, Rigaku D/Max-2000) with $\text{Cu-K}\alpha$ radiation ($\lambda = 1.5418 \text{ \AA}$). The specific surface area and pore size distribution curves of all samples were calculated from the N_2 adsorption and desorption isotherms obtained using the ASAP 2010 Accelerated Surface Area and Porosimetry System (Micrometitics, Norcross, GA).

2.4 Electrochemical performance tests

The working electrodes were prepared by mixing 80 wt % samples as active materials, 10 wt % carbon black as a conductive agent and 10 wt % polyvinylidene fluoride as a binder (PVDF) in an *N*-methyl-2-pyrrolidone (NMP) solvent. The mixture was ground to form a slurry and then blade-coated onto the graphite collectors. The working electrodes were obtained under vacuum at 80 °C overnight. The mass weight of the active materials used in the electrochemical measurements in this work was approximately 1~2 mg cm⁻². In a typical three-electrode system, measurements of the electrochemical performance, such as cyclic voltammetry (CV), galvanostatic charge/discharge (GCD), and electrochemical impedance spectroscopy (EIS, the frequency range of 10 mHz~100 kHz with a bias voltage of 10 mV), were carried out on a CHI660E electrochemical workstation (Chenhua, Shanghai) with 6 M KOH as the electrolyte solution, the prepared electrode as the working electrode, platinum foil as the counter electrode and Ag/AgCl (3 M KCl) as the reference electrode. All of the specific capacitance values (C_s , F g⁻¹) were calculated from the GCD curves using the following equation [16]:

$$C_s = \frac{It}{m\Delta V}$$

$$C_s = \frac{\int idV}{2 \times m \times \Delta V \times S}$$

where I (A) represents the charge/discharge current, t (s) is the discharge time, m (g) is the active material mass of the single working electrode in the typical three-electrode system, and ΔV (V) is the window voltage. The asymmetric supercapacitor devices (ASCs) were assembled using CMO@NC samples as the cathodic electrode and active carbon (AC) as the anodic electrode. The AC electrode was prepared by casting a mixture containing commercial AC (80 wt %), acetylene black (10 wt %), and polytetrafluoroethylene (10 wt %) onto the surface of graphite collectors. The mass of AC was calculated according to the following equation [17, 18]:

$$\frac{m_+}{m_-} = \frac{C_- \times \Delta V_-}{C_+ \times \Delta V_+}$$

where m_+ , C_+ , ΔV_+ and m_- , C_- , ΔV_- represent the mass of electrode materials, specific capacitance, and voltage window for cathodic and anodic electrodes, respectively.

The average total mass of the AC and CMO@NC was 3.5 mg cm⁻². The electrochemical performance of ASCs was measured using two electrode system with an electrochemical work station (CHI 660E) in 6 M KOH. The energy density (E) and power density (P) of the device were evaluated by the following equations [19, 20]:

$$E = \frac{C\Delta V^2}{2}$$

$$P = \frac{E}{\Delta t}$$

where C is the specific capacitance (F g⁻¹) of the ASCs, ΔV represents the discharge voltage excluding the IR drop, and Δt is the discharge time.

3. RESULTS AND DISCUSSION

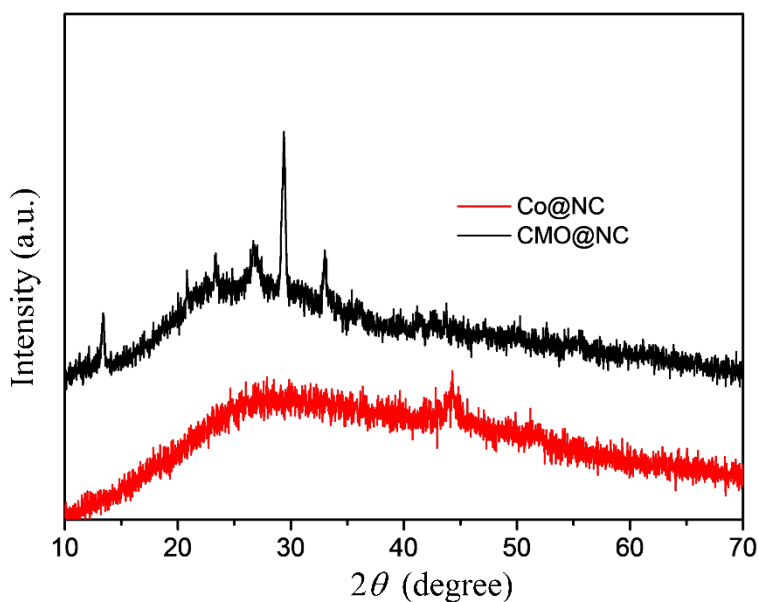


Figure 1. XRD patterns of Co@NC and CMO@NC samples.

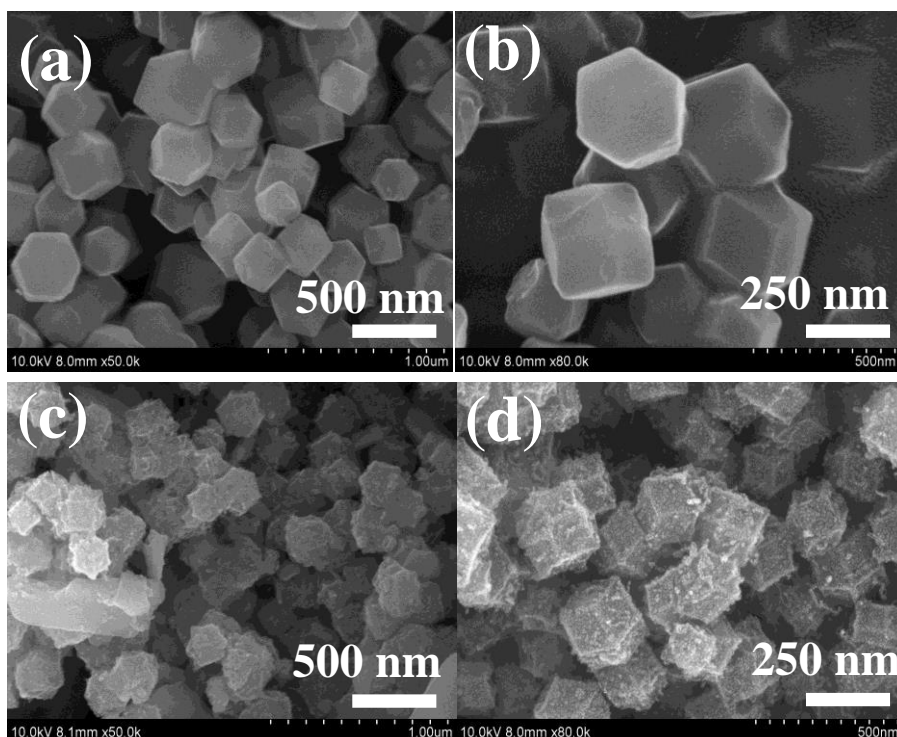


Figure 2. SEM images of the as-prepared (a, b) ZIF-67 precursor and (c, d) CMO@NC.

The crystal structures of the Co@NC and CMO@NC samples were characterized by XRD analysis, and the results are shown in Fig. 1. The corresponding XRD patterns of Co@NC located 44.2° and 51.5° can be readily indexed to metal Co (JCPDS no. 15-0806), which proves that ZIF-67 was converted to Co under a nitrogen atmosphere at high temperature [21]. After reaction with

$\text{Na}_2\text{MoO}_4 \cdot 2\text{H}_2\text{O}$, peaks at approximately 13.4° , 23.4° , 26.4° , 29° and 32.2° , which correspond to JCPDS card No. 21-0868, were observed, indicating that CoMoO_4 was formed [22, 23]. At the same time, N-doped carbon was formed under high temperature from organic linkers, which could be proven from the XRD pattern peak located at approximately 24° .

As shown in Figs. 2 (a) and (b), the as-prepared ZIF-67 has a regular polyhedral structure with a smooth surface and a size distribution of 300~350 nm. Figs. 2 (c) and (d) show the images of the CMO@NC sample. After carbonization and reaction, the smooth surface of ZIF-67 became rough and uneven, and the nanoparticles were attached onto the surface of the polyhedrons, while the particle size of the polyhedron slightly decreased. It is worth noting that the morphology remained unchanged, demonstrating the structural stability of the MOFs.

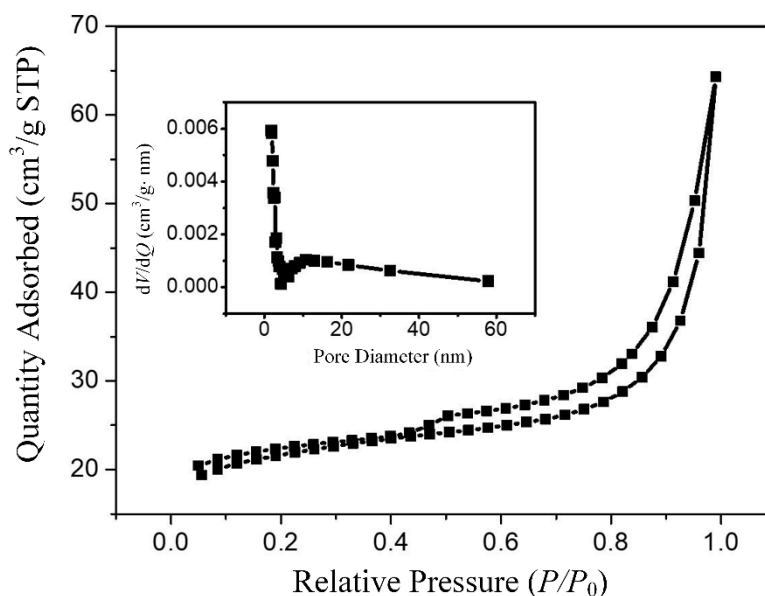


Figure 3. Nitrogen adsorption-desorption curves, and the inset is the pore size distributions of CMO@NC.

Fig. 3 depicts the N_2 adsorption-desorption curves of the sample, which present a typical type IV isotherm with a hysteresis loop for adsorption. The BET specific surface area and pore volume of CMO@NC were $69.32 \text{ m}^2 \text{ g}^{-1}$ and $0.66 \text{ cm}^3 \text{ g}^{-1}$, respectively. At the same time, it can be seen from the inset of Fig. 3 that the pore size distribution of the CMO@NC sample was mainly concentrated at 4~5 nm, showing a typical mesoporous structure with few macropores [24, 25]. A large specific surface area and pore volume as well as a reasonable pore size are conducive to the rapid diffusion of electrolyte ions and significantly improve the utilization rate of active sites of electrode materials [26].

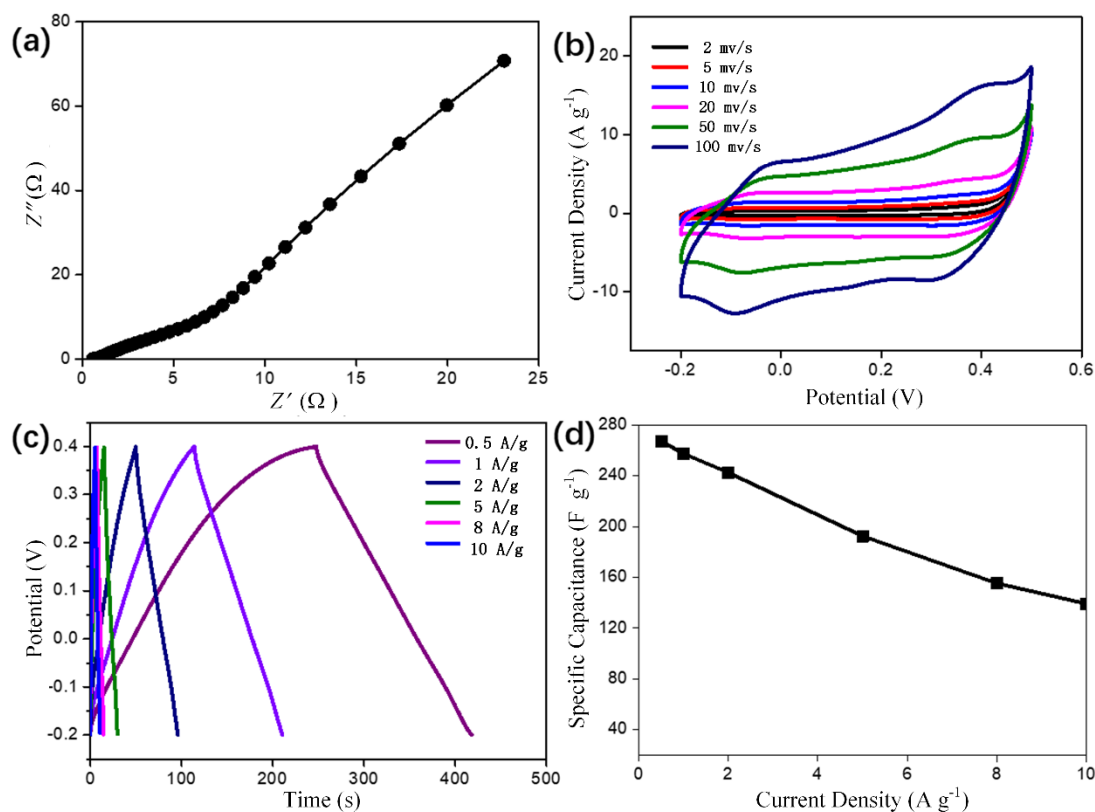


Figure 4. Electrochemical performance of the CMO@NC sample for supercapacitors: (a) Nyquist plots, (b) CV curves at different scan rates, (c) GCD curves at various current densities, and (d) specific capacitance as a function of discharge current density.

The electrochemical performance of CMO@NC was tested by means of an electrochemical workstation in a three-electrode system in a 6 M KOH solution. Fig. 4 (a) shows that CMO@NC has very small values of R_{ct} (0.3Ω). This indicates that the charge transfer of the electrode material interface in the electrochemical process can be facilitated by the CMO wrapped by N-doped carbon; thus, a higher capacitance and faster interfacial redox reaction rate can be obtained. Fig. 4 (b) shows the CV curve of CMO@NC, with a sweep rate from 2 to 100 mV s^{-1} in a voltage range of $-0.2 \sim 0.5 \text{ V}$. Each curve contains a pair of redox peaks at -0.05 and 0.35 V , which corresponds to the $\text{Co}^{2+}/\text{Co}^{3+}$ transformation, indicating that the material is a battery-operated material [27, 28]. When the scanning speed was increased, the peak current of each curve also increased, which indicates that the transmission rate of electrons and electrolyte ions was not affected by the change in scanning speed. At the same time, the shape of each CV curve did not change significantly, indicating that the CMO@NC electrode could maintain a high degree of reversibility during rapid charging-discharging [29, 30]. Fig. 4(c) presents the curves of the CMO@NC electrode charging-discharging voltage changing with time under different current densities from 0.5 A g^{-1} to 10 A g^{-1} . The asymmetric curves show that CMO acts as a pseudocapacitor in the process of constant current charge and discharge. According to the discharge time of the GCD curve in Fig. 4 (c), the specific capacitance under different current densities can be calculated (Fig. 4 (d)). When the discharge current density is $0.5, 1, 2, 5, 8$ and 10 A g^{-1} , the specific capacitance was $267.3, 257.5, 242.6, 192.5, 155.4$ and 139.2 F g^{-1} , respectively.

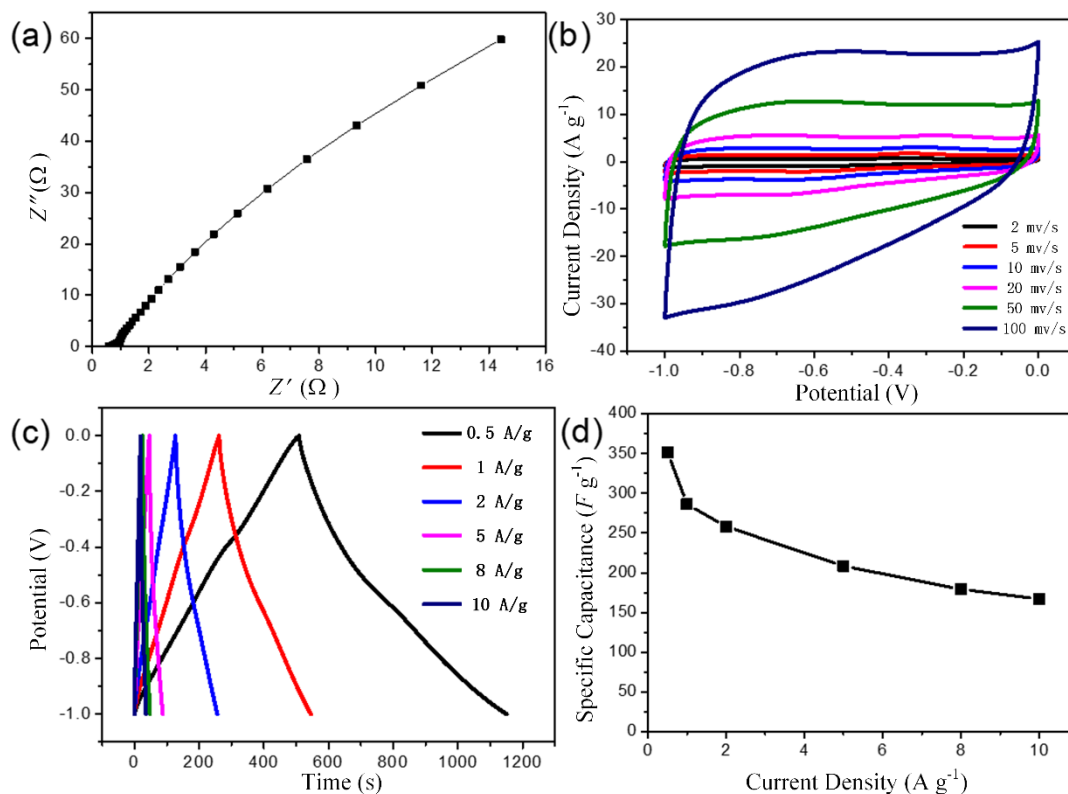


Figure 5. Electrochemical performance of the AC electrode for supercapacitors: (a) Nyquist plots, (b) CV curves at different scan rates, (c) GCD curves at various current densities, and (d) specific capacitance as a function of discharge current density.

Fig. 5 (a) shows the Nyquist plot of the AC electrode, consisting of a diagonal line in the low-frequency region and a small arc in the high-frequency region. The diameter of the circle in the high-frequency area represents the R_{ct} value between the AC electrode materials and electrolyte interface. After fitting, the value was 0.14Ω . The ultrasmall R_{ct} values indicate that the AC samples have ultrahigh electron conductivity, which is conducive to rapid charge transfer between the electrode material and electrolyte interface. The inclined line in the low-frequency area represents the Warburg impedance of ions in the electrolyte controlled by diffusion [9]. A larger slope corresponds to faster ion diffusion, which can better reflect the capacitive and reactance characteristics [31, 32]. Because the AC electrode has a very large pore volume and a reasonable pore size distribution, the curve shows a high slope, which is conducive to the rapid diffusion of ions. In Fig. 5 (b), the test voltage window is $-1 \sim 0$ V, and the CV curve presents an irregular rectangle under different scanning velocities. This was mainly because the doping of nitrogen atoms resulted in the electrode material producing a pseudocapacitor during the charging-discharging process. At the same time, it is worth nothing that when the sweep rate increased to 50 mV s^{-1} , there was no significant peak of hydrogen and oxygen evolution in the CV curve, indicating that the AC electrode was used as the electrode material of the supercapacitor with a stable chemical structure to meet the actual demand of rapid charging and discharging [33-35]. As shown in Fig. 5 (c), the GCD curves of the AC electrode show a triangular shape, and the good symmetry indicates that reversible adsorption and desorption can occur on the surface of the electrode material. In Fig. 9 (d), the

specific capacitance of the AC electrode at different discharge current densities can be calculated according to the GCD curves. When the current density was 0.5, 1, 2, 5, 8 and 10 A g⁻¹, the specific capacitance obtained was 351.9, 286.3, 258.1, 208.5, 179.2 and 167 F g⁻¹. When the current density increased by 20 times, a capacitance retention rate of 47.5 % could still be obtained.

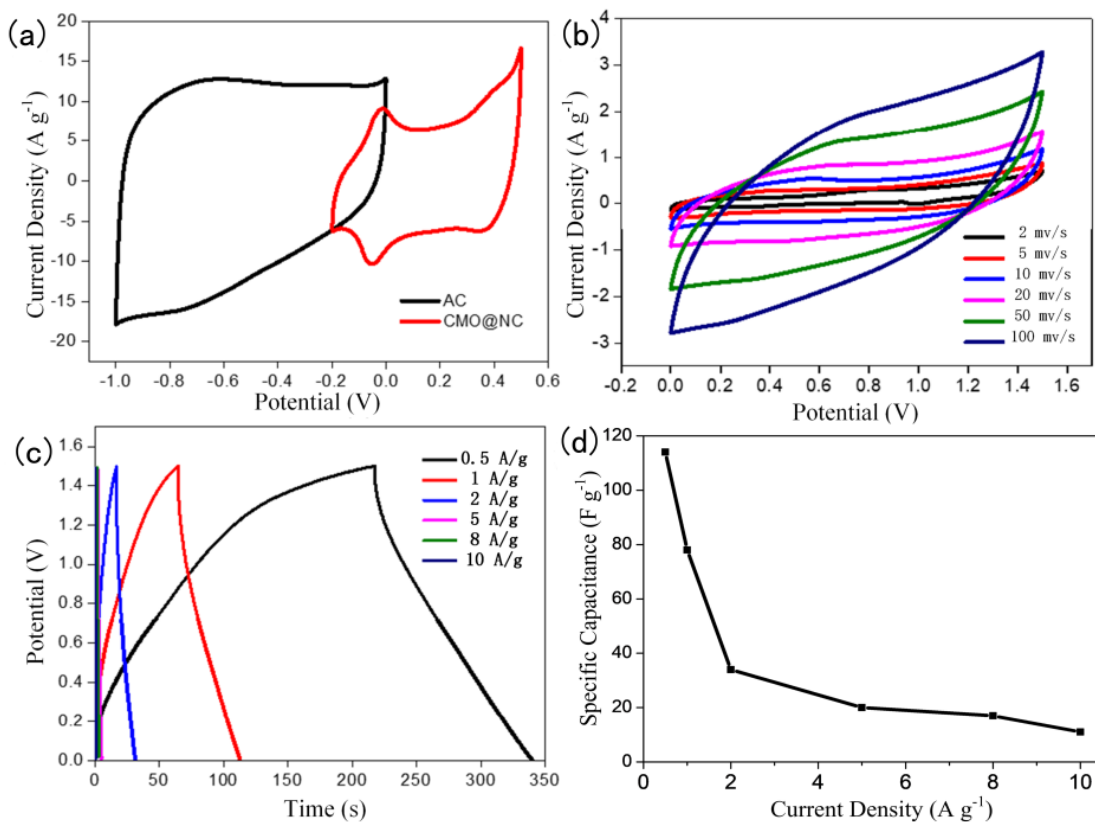


Figure 6. (a) CV curves of the CMO@NC electrode and AC electrode at 20 mV s⁻¹ measured in three-electrode system, (b) CV curves of hybrid supercapacitor at different scan rates with a voltage window of 0~1.5 V, (c) GCD curves of the HSC device collected at different current densities, and (d) specific capacitance as a function of discharge current density of hybrid supercapacitor.

To study the electrochemical characteristics of the above two electrode materials in practical applications, a CMO@NC sample was used as the positive electrode material, and an active carbon sample was used as the negative electrode material to assemble a hybrid ultracapacitor. As shown in Fig. 6 (a), the voltage windows of the active carbon electrode and CMO@NC sample electrode in the three-electrode system test were -1.0~0 V and -0.2~0.5 V, respectively. Fig. 6 (b) and (c) show the CV curves at various scanning rates and GCD curves for different voltage windows. The stable voltage window of the hybrid supercapacitor was 1.5 V. From Fig. 6 (b), we can see that the CV curves under different scanning velocities all show similar shapes, and no oxygen evolution peak appeared with an increase in scanning velocities, which indicates that 1.5 V is a relatively appropriate voltage window [36, 37]. In addition, the prominent peaks in the CV curve were caused by the redox reaction of CMO as a battery-

type electrode material. Similarly, it was found in the GCD curve (Fig. 6 (c)) that there was a weak voltage platform in the charge-discharge curve, which further confirmed the important role of CMO in hybrid supercapacitors. Fig. 6 (d) shows the specific capacitance as a function of the discharge current density of the hybrid supercapacitor. According to the total mass of the two electrode materials and the GCD curve, the specific capacitance of the hybrid device was calculated to be 114, 78, 34, 20, 17 and 11 F g⁻¹ at current densities of 0.5, 1, 2, 5, 8 and 10 A g⁻¹, respectively. To explore the cyclic stability of the active carbon//CMO@NC hybrid supercapacitors, the charge-discharge characteristics were tested at a current density of 10 A g⁻¹. As seen from Fig. 7 (a), the selected GCD curves of the 1st, 1000th, 2000th, 3000th, 4000th and 4900th cycles show a similar trend, which further demonstrates the cycling stability of the hybrid device [38, 39]. Fig. 7 (b) shows that the specific capacitance retention of the hybrid device shows an unchanged trend at the beginning of 2000 cycles, indicating the stability of the electrode materials. After a long cycle test of 5000 cycles, the specific capacitance of the hybrid supercapacitor remained at approximately 82.4 %, which proves that the equipment has an excellent long cycle stability. Furthermore, we designed and assembled a pouch cell via the two hybrid devices that could light the four LED (red) lights (inset of Fig. 7 (b)). Fig. 8 shows the Ragone curve of the active carbon//CMO@NC hybrid supercapacitor, which is used to describe the relationship between the power density and the energy density. It can be observed that when the capacitor had a power density of 1041 W kg⁻¹, an energy density of 35.4 Wh kg⁻¹ was obtained; when the power density was 9400 W kg⁻¹, the energy density of the capacitor still reached 6.25 Wh kg⁻¹, which is higher than some reported in the literature, as shown in Table 1. This fully proves that the assembled hybrid supercapacitor can achieve not only high power density but also ultrahigh energy density [40].

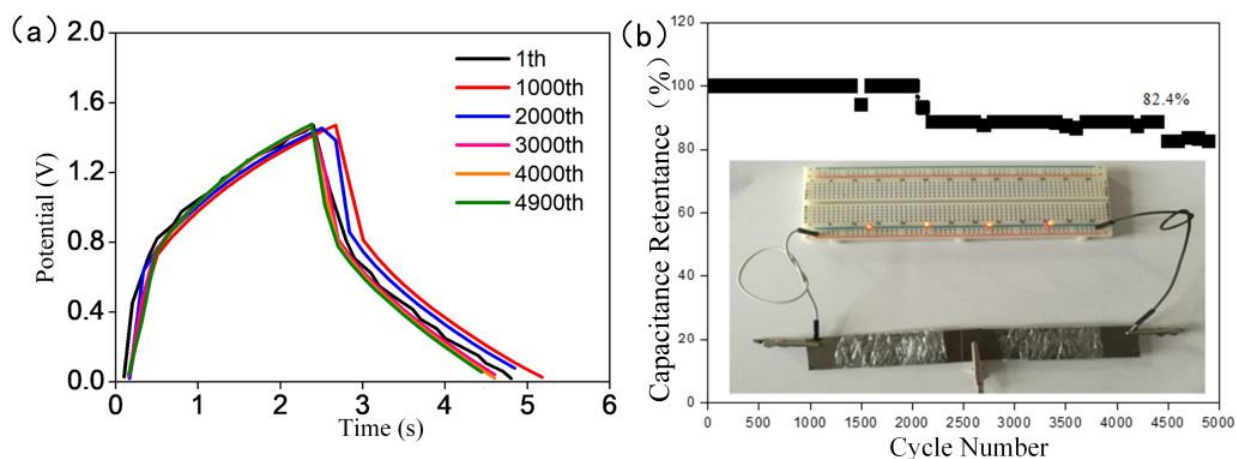


Figure 7. (a) The selected GCD curves of the 1st, 1000th, 2000th, 3000th, 4000th and 4900th cycles for the hybrid supercapacitor; (b) cycling performance of the hybrid supercapacitor device at a current density of 10 A g⁻¹; the inset shows a digital photo of the pouch cell lighting LED.

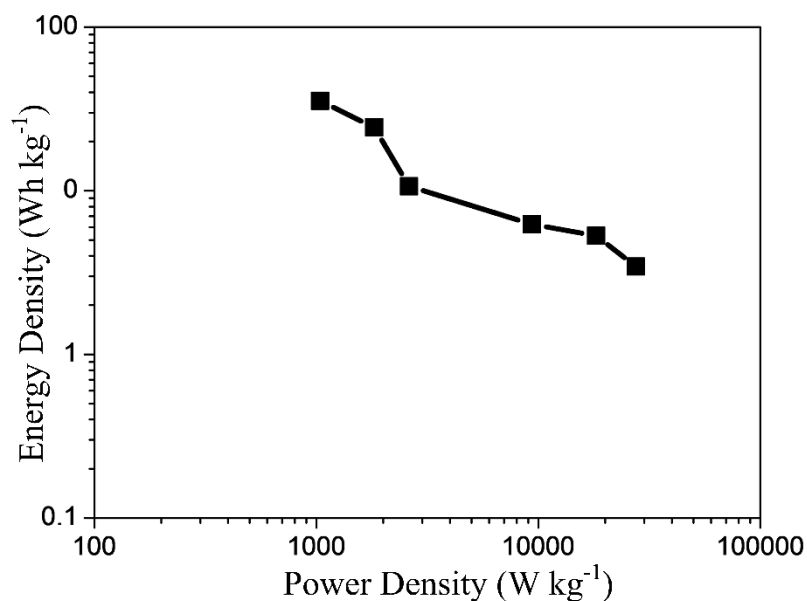


Figure 8. Ragone plots of fabricated CMO//AC asymmetric supercapacitors.

Table 1. Comparison of the energy storage parameters of ASC devices reported in the literature with those of the present CMO@NC electrode.

Samples	Energy Density (Wh kg ⁻¹)	Power Density (W kg ⁻¹)	Ref.
Mo-doped Co ₉ S ₈ porous nanosheets	14.68	369	[41]
3D CuCo ₂ O ₄ @Co(OH) ₂ core-shell	19.2	350	[42]
Bimetallic Co-Mn perovskite fluorides	8.0	140	[43]
ZIF-67-derived hollow Ni-Co layered double hydroxide	27.5	375	[44]
Co(CO ₃) _{0.5} (OH)/Ni ₂ (CO ₃)(OH) ₂ nanobelts	22.7	24019	[45]
Hierarchical Co ₃ O ₄ /CoS/Ni(OH) ₂ nanocomposite	24.5	81.8	[46]
Ni-, Co- and Mn-doped SnS ₂ -graphene aerogels	18.02	1550	[47]
Ni(OH) ₂ ultrathin nanosheets@MOF-derived Co/C nanocomposites	33.6	516.3	[48]
Biocarbon supported Ni-Co layered double hydroxide	23.5	959.7	[49]
Co(OH) ₂ /graphene	19.3	187.5	[50]
CMO@NC electrode	35.4	1041	Our work

4. CONCLUSION

In summary, the hollow structure of Co-MOFs was synthesized by adjusting the concentration of the reaction solution and using the Ostwald curing process, and then the carbon-coated hollow

structure of the CMO@NC hybrid material was obtained after high-temperature carbonization. The material shows excellent electrochemical characteristics due to its excellent electronic conductivity and unique structure. Then, hybrid supercapacitors were assembled using CMO@NC as the positive electrode material and active carbon as the negative electrode material. When the discharge current density was 1 A g^{-1} , the specific capacity was 59.3 F g^{-1} . At the same time, when the power density was 1041 W kg^{-1} , an ultrahigh energy density of 35.4 Wh kg^{-1} was obtained.

ACKNOWLEDGMENT

This work was supported by the Research Team of Anhui Provincial Education Department (2016SCXPTTD), the Key Projects of Natural Science Research of Anhui Provincial Department of Education (KJ2019A0674), the Natural Science Foundation of Anhui Province (2008085ME150) and the Key Discipline of Material Science and Engineering of Suzhou University (2017XJZDXK3).

References

1. X. Xu, Y. Liu, M. Wang, C. Zhu, T. Lu, R. Zhao, and L. Pan, *Electrochim. Acta*, 193 (2016) 88.
2. Y. Li, G. Zhu, H. Huang, M. Xu, T. Lu, and L. Pan, *J. Mater. Chem. A*, 7(2019) 9040.
3. Y. Li, W. Ou-Yang, X. Xu, M. Wang, S. Hou, T. Lu, Y. Yao, and L. Pan, *Electrochim. Acta*, 271 (2018) 591.
4. Q. Ke, C. Tang, Z. C. Yang, M. Zheng, L. Mao, H. Liu, and J. Wang, *Electrochim. Acta*, 163 (2015) 9-15.
5. M. C. Liu, L. B. Kong, C. Lu, X. M. Li, Y. C. Luo, and L. Kang, *Mater. Lett.*, 94 (2013) 197.
6. Q. Li, Y. Li, J. Zhao, S. Zhao, J. Zhou, C. Chen, K. Tao, R. Liu, and L. Han, *J. Power Sources*, 430 (2019) 51.
7. X. Geng, Y. Ai, and G. Shen, *Prog. Nat. Sci. Mater.*, 26 (2016) 243.
8. L. Zhang, S. Zheng, L. Wang, H. Tang, H. Xue, G. Wang, and H. Pang, *Small*, (2017) 1700917.
9. G. K. Veerasubramani, K. Krishnamoorthy, and S. J. Kim, *J. Power Sources*, 306 (2016) 378.
10. S. H. Kazemi, M. Tabibpour, M. A. Kiani, and H. Kazemi, *RSC Adv.*, 6 (2016) 71156.
11. X. Zhang, X. Gao, Z. Wu, M. Zhu, Q. Jiang, S. Zhou, K. Hong, and Z. Rao, *Chem. Phys.*, 523 (2019) 124.
12. X. Han, S. Liu, L. Shi, S. Li, Y. Li, Y. Wang, W. Chen, X. Zhao, and Y. Zhao, *Ceram. Int.*, 45 (2019) 14634-14641.
13. M. X. Wang, J. Zhang, H.L. Fan, B.X. Liu, X.B. Yi, and J. Q. Wang, *New J. Chem.*, 43 (2019) 5666-5669.
14. X. T. Li, Z. Q. Hu, , and P. F. Jia, *New Chem. Mater.*, 41 (2013) 92.
15. D. Guo, P. Zhang, H. Zhang, X. Yu, J. Zhu, Q. Li, and T. Wang, *J. Mater. Chem. A*, 1 (2013) 9024.
16. X. W. Dong, Y. Y. Zhang, W. J. Wang, and R. Zhao, *J. Alloy. Compd.*, 729 (2017) 716.
17. J. Jiang, Y. Sun, Y. Chen, X. Hu, L. Zhu, H. Chen, and S. Han, *J. Mater. Sci.*, 54 (2019) 11936.
18. W. Zhao, B. Hu, Q. Yang, Z. Wang, X. Li, Y. Jin, Y. Xi, J. Li, and W. Q. Tian, *Carbon*, 150 (2019) 371.
19. M. Li, Y. Wang, H. Yang, and P. K. Chu, *J. Mater. Chem. A*, 5 (2017) 17312.
20. Y. Jiang, X. Zheng, X. Yan, Y. Li, X. Zhao, and Y. Zhang, *J. Colloid Interf. Sci.*, 493 (2017) 42.
21. G. Lee, W. Na, J. Kim, S. Lee, and J. Jang, *J. Mater. Chem. A*, 7 (2019) 17637.
22. G. Jiang, L. Li, Z. Huang, Z. Xie, and B. Cao, *J. Alloy. Compd.*, 790 (2019) 891.
23. J. Wang, J. Chang, L. Wang, and J. Hao, *Ionics*, 24 (2018) 3967.

24. X. Zhang, W. Qin, D. Li, D. Yan, B. Hu, Z. Sun, and L. Pan, *Chem. Commun.*, 51 (2015) 16413.
25. X. Zhang, W. Ou-Yang, G. Zhu, T. Lu, and L. Pan, *Carbon*, 143 (2019) 116.
26. X. Y. Gao, G. Zhu, X. J. Zhang, and T. Hu, *Micropor. Mesopor. Mater.*, 273 (2019) 156.
27. Y. Zhao, X. He, R. Chen, Q. Liu, J. Liu, D. Song, H. Zhang, H. Dong, R. Li, M. Zhang, and J. Wang, *Appl. Surf. Sci.*, 453 (2018) 73.
28. M. Li, H. Yang, Y. Wang, L. Wang, and P. K. Chu, *Electrochim. Acta*, 283 (2018) 538.
29. J. Xie, Z. Zhan, S. Zhang, G. Li, H. Xia, Y. Yang, and J. Xiong, *Mater. Lett.*, 226 (2018) 30.
30. Y. Feng, W. Liu, L. Sun, Y. Zhu, Y. Chen, M. Meng, J. Li, J. Yang, Y. Zhang, and K. Liu, *J. Alloy. Compd.*, 753 (2018) 761.
31. Q. Gao, *J. Energy Chem.*, 38 (2019) 219.
32. P. Liu, Q. Ru, P. M. Zheng, Z. L. Shi, Y. Liu, C. Q. Su, X. H. Hou, S. C. Su, and F. C. C. Ling, *Chem. Eng. J.*, 374 (2019) 29.
33. S. Luan, W. Li, X. Hou, Z. Guo, W. Li, Y. Song, X. Zhang, and Q. Wang, *Carbon*, 151 (2019) 18.
34. S. Sun, B. Ding, R. Liu, and X. Wu, *J. Alloy. Compd.*, 803 (2019) 401.
35. L. N. Kong, W. Yang, L. Su, S. G. Hao, G. J. Shao, and X. J. Qin, *Ionics*, 25 (2019) 4333.
36. M. Ghaemmaghami, and R. Mohammadi, *Sustain. Energy Fuels*, 3 (2019) 2176.
37. Y. Zhao, Y. Liu, J. Du, X. Zhang, J. Zhou, X. Li, C. Wu, Z. Zhu, E. Xie, and X. Pan, *Surf. Sci.*, 487 (2019) 442.
38. F. Liu, Y. Yang, S. Li, T. Chen, H. Long, H. Wang, and M. Liu, *J. Mater. Sci. Mater. Electron.*, 29 (2018) 10353.
39. S. J. Patil, and D. W. Lee, *J. Mater. Chem. A*, 6 (2018) 9592.
40. H. Long, T. Liu, W. Zeng, Y. Yang, and S. Zhao, *Ceram. Int.*, 44 (2018) 2446.
41. X. Zhou, Y. Ren, Y. Lu, Z. Cheng, W. Wang, Q. Wang, W. Huang, and X. Dong, *Adv. Mater. Interfaces*, 6 (2019) 1901138.
42. Y. Zhang, H. Liu, M. Huang, J. M. Zhang, W. Zhang, F. Dong, Y. X. Zhang, *Chem. Electro. Chem.*, 4 (2017) 721.
43. W. Shi, R. Ding, X. Li, Q. Xu, D. Ying, Y. Huang, and E. Liu, *Chem. Eur. J.*, 23 (2017) 15305.
44. P. Wang, Y. Li, S. Li, X. Liao, and S. Sun, *J. Mater. Sci.: Mater. Electron.*, 28 (2017) 9221.
45. G. Zhang, P. Qin, R. Nasser, S. Li, P. Chen, and J. Song, *Chem. Eng. J.*, 387 (2020) 124029.
46. Z. Zhu, Y. Zhou, S. Wang, C. Zhao, Z. Li, G. Chen, and C. Zhao, *Electrochim. Acta*, 284 (2018) 444.
47. H. Chu, F. Zhang, L. Pei, Z. Cui, J. Shen, and M. Ye, *J. Alloys Compd.*, 767 (2018) 583.
48. X. Li, Y. Qiao, C. Wang, T. Shen, X. Zhang, H. Wang, Y. Li, and W. Gao, *J. Alloys Compd.*, 770 (2019) 803.
49. D. Zhang, X. Guo, X. Tong, Y. Chen, M. Duan, J. Shi, C. Jiang, L. Hu, Q. Kong, and J. Zhang, *J. Alloys Compd.*, 837 (2020) 155529.
50. C. Zhao, F. Ren, X. Xue, W. Zheng, X. Wang, and L. Chang, *J. Electroanal. Chem.*, 782 (2016) 98.